

X-ray Absorption in Insulators with Non-Hermitian Real-Time Time-Dependent Density Functional Theory

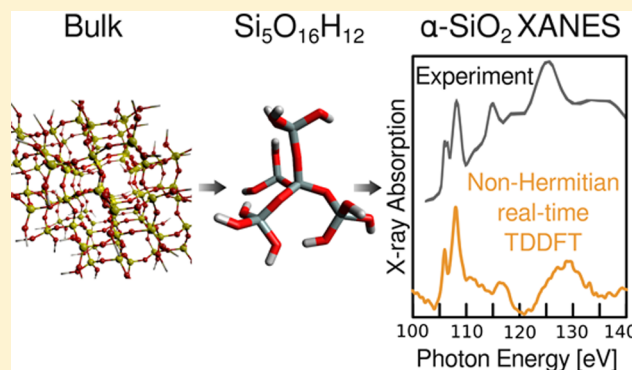
Ranelka G. Fernando,[†] Mary C. Balhoff,[†] and Kenneth Lopata^{*,†,‡}

[†]Department of Chemistry, Louisiana State University, Baton Rouge, Louisiana 70803, United States

[‡]Center for Computation & Technology, Louisiana State University, Baton Rouge, Louisiana 70803, United States

Supporting Information

ABSTRACT: Non-Hermitian real-time time-dependent density functional theory was used to compute the Si L-edge X-ray absorption spectrum of α -quartz using an embedded finite cluster model and atom-centered basis sets. Using tuned range-separated functionals and molecular orbital-based imaginary absorbing potentials, the excited states spanning the pre-edge to ~ 20 eV above the ionization edge were obtained in good agreement with experimental data. This approach is generalizable to TDDFT studies of core-level spectroscopy and dynamics in a wide range of materials.



1. INTRODUCTION

X-ray absorption spectroscopy (XAS) is an important tool for chemistry and solid-state materials as it provides information on charge, bonding, and oxidation states of a particular atom. XAS involves the transition of a core-level electron to either bound or continuum states and is broadly characterized as pre-edge, X-ray absorption near-edge structure (XANES), and extended X-ray absorption fine structure (EXAFS).¹ Pre-edge is the region below the binding energy of the core level, whereas the near-edge region (XANES) contains features up to 50 eV above the binding energy. Photoelectrons in the XANES region have low kinetic energy and excited states in this region involve multiple scattering, which is useful for obtaining three-dimensional structural information.¹ XANES spectra are often complex and modeling these excitations is crucial for interpreting experimental results. Moreover, an accurate description of these excited states is an important first step toward understanding X-ray triggered dynamics in materials.

Several techniques have been used to model XAS. The multiple scattering approach,^{2,3} which is perhaps the most widely used method for XAS, treats the photoelectron as spherical waves scattering from muffin-tin potentials. This has been widely used to study EXAFS in materials, but XANES can be challenging for these techniques as it requires experimental parametrization and can lack a rigorous treatment of the electronic structure of the material. XAS can also be calculated using first principles, such as Bethe–Salpeter equation (BSE)-based methods,^{4,5} where core–hole interactions are described via a two-particle picture. BSE offers a much improved picture of the virtual states but can become extremely time consuming for large supercells, for example, in materials with defects or disorder.

Alternatively, one can use core–hole pseudopotentials in conjunction with band structure-based first-principles methods such as single-particle approximations based on density functional theory (DFT).⁶ This has been used to capture XANES of lithium and fluorine *K*-edges of LiF and carbon *K*-edge of diamond⁷ and the *K*-edges of silicon and oxygen in α -quartz.⁶ Although this method generates the XAS up to the far edge region and is suitable for weakly coordinated systems, it shows limitations in moderate and strong correlation environments. These deficiencies in the electron–electron interactions in the DFT functional can be somewhat remedied using the DFT + *U* method.⁸ In addition to this, modeling transition metals and rare earths require large kinetic energy cutoffs that can result in excessive computational time. Ultrasoft pseudopotentials based on DFT methods have also been used to compute the XAS of silicon and oxygen *K*-edges of α -quartz and copper *K*-edge spectra in Cu and in La_2CuO_4 .⁸

Finally, core excitations can be modeled using DFT using the Kohn–Sham approach, but this requires computing each core excited state one-by-one, which becomes computationally expensive and time consuming for materials.⁹ TDDFT on the other hand can be used to generate XANES spectra from a single calculation, as discussed later. A combination of TDDFT with BSE can also offer information on a wide spectral range above the edge.^{10–13}

In this paper, we develop an alternative approach to post-edge XANES using real-time time-dependent DFT (RT-TDDFT) with atom-centered basis sets. The goal is to accurately describe excitations near and above the edge of

Received: October 23, 2014

wide-gap materials without any parametrization against experiment. In many ways, this is a complementary approach to the methods discussed above but has the added bonus of easily handling doping/disorder,¹⁴ allows for efficient use of hybrid DFT functionals, and easily translates to dynamical simulations, for example, X-ray-induced dynamics and strong-field effects.¹⁵

Time-dependent DFT¹⁶ is an excellent approach for modeling these processes as it offers a good description of the electronic structure for transition metal systems and materials. A suitable choice of DFT functional yields excitations over a wide range of energies, scales to large system sizes (suitable for defect sites, surfaces, or disordered systems), and is a natural tool for modeling dynamics. For an overview of TDDFT and its myriad of applications, see the reviews by Marques and Gross,¹⁷ Burke,¹⁸ Casida,¹⁹ and Ullrich.²⁰ Despite its wide applicability, capturing above-ionization core-level excitations can be challenging for TDDFT for two reasons: inadequacies in atom-centered basis sets and failures of traditional exchange-correlation functionals for high energy states.^{21–25} Both these issues stem from the highly diffuse Rydberg or continuum-like virtual states involved in these excitations.

These states are poorly described by atom-centered basis sets, yet grids and planewaves, which are ideal for diffuse states, can be problematic for the wave function near the core. This can be remedied somewhat through the use of excited-state core–hole pseudopotentials.^{26,27} Atom centered basis sets such as Gaussian type orbitals (GTOs), however, are often preferred over planewaves due to their computational efficiency with hybrid functionals. Specifically, the Hartree–Fock wave function component is nonlocal in space and scales as N^4 , which can become prohibitively expensive for planewaves that can easily have hundreds of times more functions than GTO basis sets. Local density functionals (e.g., LDAs, GGAs) are unsuitable for capturing above-ionization as they have the incorrect asymptotic form of the potential and qualitatively fail to describe the excitations. To overcome this problem, range-separated functionals such as CAM-B3LYP,²⁸ BNL,²⁹ LC-PBE,³⁰ LC-PBE0,³¹ etc. have been developed that incorporate both long-range and short-range parts into the exchange term in the Kohn–Sham energy functional. These functionals provide robust and more successful solutions to self-repulsion that occur at long ranges.^{30,32–35}

Thus, we would expect a versatile TDDFT approach to use GTOs with range-separated functionals yet also adequately describe the large spatial extent of the continuum-like states. One way forward is to use imaginary absorbing boundary conditions (ABCs) that mimic the continuum. Typically, this is done in real space, where the potentials take the form of a slowly increasing function at the simulation box edge that removes the wave function without artificial reflections from the edge of a numerical grid.^{36–38} This technique has been widely successful in modeling resonance energies and lifetimes.^{39,40} Absorbing potentials have also been used with multireference configuration interaction to study resonances of metastable dianionic species,⁴¹ resonances with coupled cluster,^{42,43} and photoabsorption oscillator strength of clusters and molecules,^{44,45} along with computing ionization rates in atoms using TDDFT.⁴⁶

These approaches can be inefficient for GTOs, as they require a very large number of diffuse functions to describe the ABC far from the molecule. Instead, we recently developed a phenomenological molecular orbital (MO)-based ABC, where

we impose a condition to mimic the finite lifetime of above ionization states by applying an imaginary potential to the Fock matrix in the MO basis, which is similar in spirit to complex DFT,⁴⁷ complex scaling,^{48–50} and linear response complex polarizability approaches.⁵¹ This MO-based ABC was successfully applied to UV resonance states in small gas-phase molecules.⁵²

Finally, solving the time-dependent Kohn–Sham equations in time domain (i.e., real-time TDDFT^{53–56}) is a natural tool for modeling XANES in materials, which requires computing spectra spanning tens of eV above the ionization edge in systems with a high density of states. Here, traditional root-based linear response TDDFT^{57,58} (LR-TDDFT) requires thousands of roots, which is both inefficient and potentially creates algorithmic stability issues. RT-TDDFT, on the other hand, requires only three simulations (x , y , z polarized) to capture the entire absorption spectrum. RT-TDDFT has similar advantages when computing spectra in disordered solids, for example, $(\text{Fe}_{1-x}\text{Cr}_x)_2\text{O}_3$ solid solutions.¹⁴

One final note concerns the use of an adiabatic (local in time) approximation to the exchange-correlation functional, which is strictly valid only for slowly varying time-dependent driving fields.⁵⁹ For fields with high frequencies or strengths, the functional at a particular time is also dependent on the density at earlier times, making “memory” effects significant.⁵⁹ Recent studies, however, have shown that for a finite electron system in its ground state gradually exposed to a high frequency field these memory effects become negligible, and thus, the adiabatic approximation remains valid.⁶⁰ This picture is consistent with the results of this paper, as well as previous TDDFT studies of X-ray absorption,⁶¹ where the computed excited states agree well with the experiment despite the use of an adiabatic functional.

TDDFT has been widely used to model XAS in a range of molecular systems such as the core excitations of Ti 1s, 2p and Cl 2p of TiCl_4 ,⁶² the chlorine and sulfur *K*-edge and molybdenum *L*-edge of oxomolybdenum complexes,⁶³ *L*₃-edge of ruthenium complexes,^{61,64,65} oxygen *K*-edge of water and carbon monoxide (CO), carbon *K*-edge of CO, and the carbon and fluorine *K*-edges of fluorobenzenes.⁶¹ TDDFT has also been used to compute the carbon 1s XAS of acetylene, ethylene, and benzene in gas phase and adsorbed on a Si(100) surface.⁶⁶ Sulfur *K*- and *L*-edges and the oxygen *K*-edge of SO_2 adsorbed on the MgO(100) surface⁶⁷ and sulfur *K*-edge of SO_2 adsorbed on the Ti(110) surface have also been studied using TDDFT.⁶⁸ Studies have been performed on XAS at *L*_{2,3} edges of 3d elements (Sc, Ti, V, Cr, Ni) of atoms and complexes using TDDFT methods.^{69,70} For materials, linear response TDDFT has been applied to metal 1s and 2p edges and oxygen 1s edges of alkaline earth metal oxides using cluster models of MgO, CaO, SrO, and BaO,⁷¹ titanium *K*- and *L*-edges and oxygen *K*-edge in rutile using finite cluster models of TiO_2 ,⁷² vanadium and oxygen *K*-edges, and vanadium *L*-edge of V_2O_5 .⁷³

In this paper, we outline a real-time TDDFT approach to XAS for materials that use bulk-mimicking finite clusters, tuned range-separated functionals, and molecular orbital ABCs to capture XANES. As an illustrative example, we apply the approach to α - SiO_2 and compare with experimental spectra. Silicon dioxide (SiO_2) is an abundant material in the Earth’s crust and mantle and has a wide range of technological applications including piezoelectrics, optical fibers, microelectronics, and, nanogenerators, to list only a few.^{74–76}

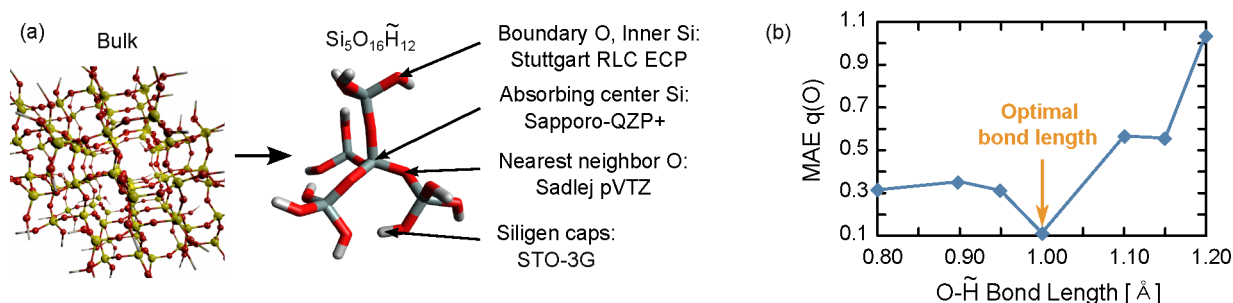


Figure 1. (a) Bulk-mimicking finite cluster of α -quartz with mixed basis set suitable for X-ray absorption studies. (b) Boundary O–H bond lengths were tuned to ensure charge consistency of the cluster.

There are several polymorphs of SiO_2 , most of which are 4-fold coordinated (α -quartz, cristobalite, tridymite, and coesite), have a tetrahedral geometry around the Si atoms, and 2-fold coordination around oxygen atoms (4:2 structures). Stishovite, on the other hand, has a 6:3 coordinated rutile-type structure with an octahedral geometry around the Si atoms.⁷⁷ Among these, α -quartz is the most stable polymorph under ambient conditions, is most important industrially, and is the most well studied experimentally and theoretically.⁷⁴ Thus, we focus on α -quartz as a simple test case for near- and post-edge XANES in insulators, and we validate our results against previous computational and experimental data.

2. RESULTS

In this paper, we use real-time TDDFT to model the X-ray absorption of α -quartz with a goal of capturing both near- and above-ionization XANES features without input from experiment. Atom-centered basis sets were used along with tuned range-separated functionals for a better description of high energy excitations. Absorbing boundary conditions were employed to emulate the continuum and reduce artifacts from the finite basis sets. We focus on α -quartz, but the approach is generalizable to similar materials. Schematically, the approach involves the following steps, which we discuss in the following subsections:

- (1) Generate a small bulk-mimicking finite cluster of α -quartz that is capped with “siligens” tuned to ensure charge consistency of the atoms (Section 2.1).
- (2) Tune LC-PBE0 range-separated functional to satisfy Koopmans’ and ΔSCF ionization potentials; test straight line behavior of functional (Section 2.2).
- (3) Construct a molecular orbital-based absorbing potential (Section 2.3).
- (4) Use real-time TDDFT to compute absorption spectrum across pre-edge and XANES regions (Section 2.4).

2.1. Bulk-Mimicking Finite Cluster. The first step is to construct a finite cluster that is carved from the bulk crystal and capped to ensure charge consistency. The trigonal unit cell of α -quartz ($a = 4.91239$ Å and $c = 5.40385$ Å) obtained from the experimental crystal structure⁷⁸ was used to build a 17 Si bulk α -quartz model ($\text{Si}_{17}\text{O}_{16}$). This structure was truncated to make a smaller spherical cluster, Si_5O_{16} , centered around a silicon atom, which will eventually become the absorbing center for the XAS calculations. The dangling bonds of the spherical structure were capped with “siligens” (H-pseudohydrogen atoms mimicking bulk Si atoms) to generate $\text{Si}_5\text{O}_{16}\tilde{\text{H}}_{12}$. As this is a 4:2 coordinated system, hydrogens passivate this cluster without needing embedding charges. The central Si atom is

thus coordinated to four bridging oxygen atoms, each of which are bonded to one boundary Si atom, which are in turn bonded to three boundary oxygen atoms, terminated by siligens. The finite cluster mimicking the bulk is shown below in Figure 1(a).

The validity of this finite cluster depends strongly on the boundary siligen atoms, which act as a “boundary condition” for the electronic structure and dictate the charge of the cluster. One simple self-contained method for choosing the boundary atoms, which avoids tuning to the experiment, is to vary the O–H bond length to ensure charge consistency of the atoms in the cluster.⁷⁹

$$|q(\text{Si})| = 2|q(\text{O})| \quad (1)$$

$$4q(\tilde{\text{H}}) = q(\text{Si}) \quad (2)$$

$$q(\text{O}_{\text{non-bridging}}) = q(\text{O}_{\text{bridging}}) \quad (3)$$

Here, for a given basis set, the O–H bond length is tuned to minimize the error/charge inconsistencies. Mulliken population analysis is unsuitable as it is highly basis set dependent and does not consider the differences in electronegativities of atoms in molecules. Instead, the charge analysis was performed using Bader analysis, which is based on the Atoms in Molecules Theory.^{80–83} This method assigns atomic “charges” (an ill-defined quality in molecules) by locating minima in the charge density and is less sensitive to basis sets than Mulliken analysis.^{83,84}

In anticipation of XAS calculations, which involve transitions from the core of a single Si atom to a delocalized state, a mixed basis with 363 functions was used where the Sapporo-QZP-2012+diffuse(all)/without G functions was used for “core” Si atom and Sadlej pVTZ (Pol1) for “bridging” oxygen atoms bound to core Si, respectively, and Stuttgart RLC ECP was used for boundary Si and O atoms. STO-3G was used for H in siligen caps. This mixed basis description with absorbing center (Si) and neighbors with large polarized functions and outer atoms with a small basis set is economical but sufficient to capture the static and excited-state properties. Convergence with the basis set was checked using Dunning-type aug-cc-pV{T,Q}Z for the optical gap.

Using this basis set and the PBE0³¹ functional, Bader analysis⁸⁰ was performed on the small cluster, ($\text{Si}_5\text{O}_{16}\tilde{\text{H}}_{12}$) for a series of O–H bond lengths (0.8 to 1.2 Å) using the Bader utility from the Henkelman group.^{80,81,83} For each fixed O–H bond length, the cluster geometry was optimized, and the mean absolute error (MAE) for “bridging” and “boundary” oxygen atoms was determined. Figure 1(b) shows that the lowest MAE for oxygen atoms is achieved when O–H bond length is 1.0 Å.

Similar analysis for the Si atoms was not performed due to extreme basis set unbalance (quadruple- ζ vs ECP).

2.2. Tuned Range-Separated Functional. Obtaining high energy excitations using TDDFT is problematic due to the incorrect asymptotic behavior of the exchange-correlation functional.^{21–25} These can be somewhat mitigated by using asymptotic correlations (e.g., LB94²¹ and CS00^{85,86}). Another solution, which has been very successful for high energy molecular excitations and charge transfer, is to use range-separated functionals. Here, the exchange term in the Kohn–Sham energy functional is divided into short-range and long-range parts:^{28,52,87}

$$E_{\text{XC}}[\rho, \{\psi\}] = E_{\text{X}}^{\text{DFT,short}}[\rho] + E_{\text{X}}^{\text{HF,long}}[\{\psi\}] + E_{\text{C}}^{\text{DFT}}[\rho] \quad (4)$$

where E_{XC} is the exchange-correlation energy, E_{X} is the exchange energy, and E_{C} is the correlation energy. Here, the exchange decomposition takes the form

$$\frac{1}{r_{12}} = \frac{\alpha + \beta \text{erf}(\mu r_{12})}{r_{12}} + \frac{1 - [\alpha + \beta \text{erf}(\mu r_{12})]}{r_{12}} \quad (5)$$

The short-range interactions use DFT exchange, and the long-range parts use Hartree–Fock exchange (HF) and potentially smoothly switches from DFT to the HF exchange. α and β are dimensionless parameters that determine the HF and DFT contributions in the long/short-range region. When $r_{12} \rightarrow 0$, the functional will retain an α fraction of HF and $(1 - \alpha)$ fraction of DFT exchange, and as $r_{12} \rightarrow \infty$, there will be an $(\alpha + \beta)$ fraction of HF and $(1 - \alpha - \beta)$ fraction of DFT exchange. The range-separation attenuation parameter, μ , determines how rapidly the DFT exchange switches to HF.

Going further, the accuracy of the functionals for excited states has been shown to be improvable by tuning α and γ self-consistently to minimize the errors in ionization energies.^{52,87} In this work, which focuses on diffuse- and above-ionization states, the range-separated functional LC-PBE0 was used to obtain the X-ray absorption spectrum of α -quartz. Similar to previous molecular studies, this functional was tuned to obtain the best parameters (α and γ), which satisfy the Koopmans' ionization potential condition ($\text{IP} = -\epsilon_{\text{HOMO}}$).^{52,87}

$$J(\mu) = |\text{IP}_{\text{SCF}}(\mu) - \text{IP}_{\text{Koopmans}}(\mu)| \quad (6)$$

$$= |E_{\text{SCF}}^{\text{cation}}(\mu) - E_{\text{SCF}}^{\text{neutral}}(\mu) + \epsilon_{\text{HOMO}}^{\text{neutral}}| \quad (7)$$

$J(\mu)$ is the object function for a neutral molecule, SCF denotes the ground-state Kohn–Sham energies, and ϵ_{HOMO} is the eigenvalue of the HOMO orbital. The resulting tuned functional is denoted as LC-PBE0*.

As shown below in Figure 2, the lowest $J(\mu)$ for α -quartz for LC-PBE0* was achieved when $\alpha = 0.515$ and $\gamma = 0.101 \text{ au}^{-1}$. The calculated Koopmans' IP and ΔSCF for these values were 11.2 and 11.1 eV, respectively, which results in 1.08% difference between the two energies.

Another important characteristic of an exchange-correlation functional is the so-called straight line behavior that measures the behavior of the energy as a function of the fractional electron number (ΔN).^{87–89} For an exact functional, the energy of the atom or molecule changes linearly between adjacent integers but results in discontinuous slopes as ΔN reaches the number of electrons in the neutral molecule where the slope switches from $-\text{IP}$ (ionization potential) to $-\text{EA}$ (electron affinity). Although functionals can be tuned to satisfy

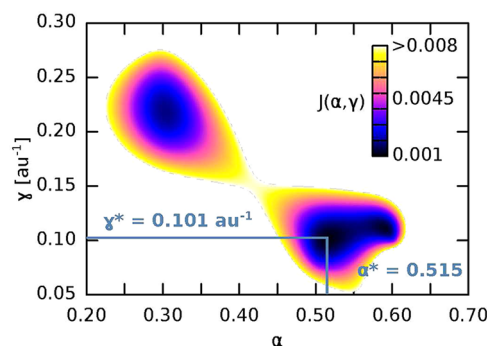


Figure 2. Tuning the LC-PBE0 range-separated functional.

this, we only tuned the ionization potential and simply checked the straight line behavior.

Figure 3 illustrates the changes in calculated energies as a function of the change in the fractional occupation number

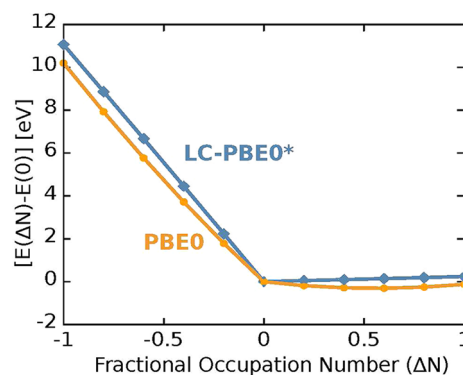


Figure 3. Straight line behavior for global hybrid (PBE0) and tuned range-separated functional (LC-PBE0*).

(FON) of the cluster ΔN , both for the tuned functional as well as the parent global hybrid PBE0. As shown in Figure 3, a clear derivative discontinuity is seen around the neutral molecule ($\Delta N = 0$) for both functionals. A nearly optimal straight line is seen for the LC-PBE0* functional at the electron deficient part ($\Delta N < 0$) as well as in the electron-rich ($\Delta N > 0$) region, and the slope changes from $-\text{IP}$ to $-\text{EA}$. In contrast to the behavior of the LC-PBE0* functional, the PBE0 functional demonstrates an incorrect convex behavior at the electron-rich part due to the delocalization errors associated with the functional. Localization errors due to nonstraight line behavior result in erroneous band gaps of materials. This is often minimized by using hybrid functionals, where errors due to convex and concave parts cancel, producing more reliable band gaps.^{89,90} Here, the functional, which avoids these issues, yielded an optical band gap (lowest LR-TDDFT root) of 8.4 eV in α -quartz, which agrees well with the experimental value (8.9 eV).⁹¹ PBE0, on the other hand, significantly underestimates the band gap (6.7 eV).

2.3. Molecular Orbital-Based Absorbing Potential. The final ingredient for computing spectra is to construct an imaginary molecular orbital (MO) absorbing potential to remove spurious high energy peaks resulting from the finite atom-centered basis sets.⁵² Although most absorbing boundary conditions take the form of a smoothly increasing potential at the simulation box edges, this approach can be problematic for atom-centered basis sets. A simple, albeit somewhat more

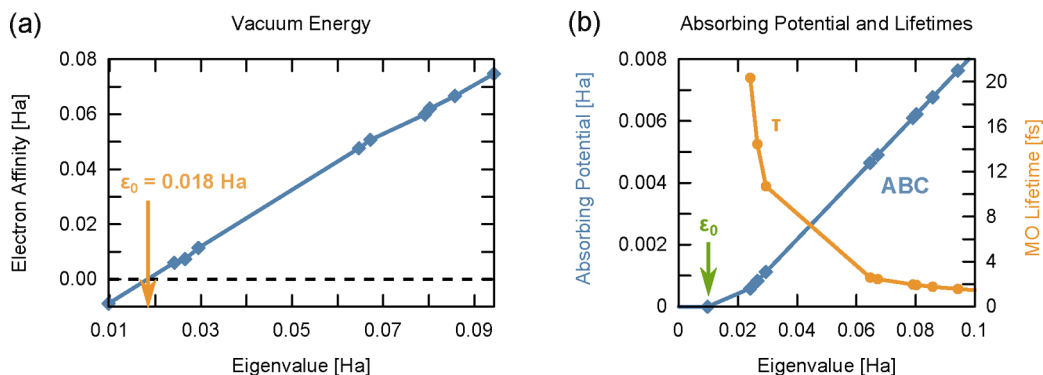


Figure 4. (a) Determination of vacuum energy cutoff (ϵ_0) via approximate electron affinities. (b) Absorbing boundary potential and corresponding molecular orbital lifetimes.

phenomenological, approach is to use absorbing boundary conditions directly in the MO space by applying an imaginary potential to the Fock matrix in the MO basis (prime notation).⁵²

$$\mathbf{F}'(t) = \mathbf{F}'_0(t) + i\mathbf{\Gamma}'(t) \quad (8)$$

where the imaginary potential, $\mathbf{\Gamma}'$ is obtained by projecting a diagonal damping matrix, \mathbf{D} , on to the instantaneous MO eigenvectors of the Fock matrix, $\mathbf{F}'_0(t)$.

$$\mathbf{\Gamma}'(t) = \mathbf{C}'(t)\mathbf{D}\mathbf{C}'^\dagger(t) \quad (9)$$

$\mathbf{C}'(t)$ denotes the matrix in which the columns are the eigenvectors of $\mathbf{F}'_0(t)$. \mathbf{D} is the diagonal damping matrix with exponentially increasing damping parameters (γ) for the MOs. The damping applied to the MOs in the continuum can take virtually any form, but we use an exponential in the eigenvalues

$$\gamma_i = \begin{cases} 0, & \tilde{\epsilon}_i \leq 0 \\ \gamma_0[\exp(\xi\tilde{\epsilon}_i) - 1], & \tilde{\epsilon}_i > 0 \end{cases} \quad (10)$$

Here, γ_i is the damping on the i^{th} MO; γ_0 defines the energy scale; ξ dictates the “steepness” of ABC; and $\tilde{\epsilon}_i = \epsilon_i - \epsilon_0$ is the energy of the i^{th} MO above the vacuum cutoff energy, ϵ_0 . This will result in τ_i lifetime in each MO

$$\tau_i = \frac{1}{2\gamma_i} \quad (11)$$

This ABC is computationally inexpensive as it needs to be constructed only once due to the relatively time-independent behavior of $\mathbf{\Gamma}'(t)$ in the limit of weak field excitations. Because this paper mainly focuses on spectroscopic data, this assumption is valid.

The vacuum energy level, ϵ_0 , can be approximated by using electron affinities (EA) of the virtual orbitals. The electron affinity of each virtual orbital (EA_k) can be calculated by combining the first electron affinity EA_1 with ν_k , which is the k^{th} LR-TDDFT excitation of the anion. Although approximate, this is a more accurate approximation to the EA than the raw Kohn–Sham virtual eigenvalues.

$$\text{EA}_1 = E^{\text{anion}} - E^{\text{neutral}} \quad (12)$$

$$\text{EA}_k \simeq \text{EA}_1 + \nu_{k-1}, \quad k = 2, 3, \dots \quad (13)$$

The eigenvalue at $\text{EA} = 0$ corresponds to ϵ_0 and can be obtained by interpolation of the eigenvalues (Figure 4(a))

which gives $\epsilon_0 = 0.018$ Ha as the cutoff energy for the finite α - SiO_2 cluster.

The imaginary potential increases exponentially with the MO eigenvalue, and the corresponding MO lifetimes decay exponentially (Figure 4(b)). This results in finite lifetimes in the low-lying unbound virtual orbitals (before they autoionize), while excitations to high-lying virtuals will be completely removed. For example, MO values 0.05 Ha above the cutoff energy have a lifetime of ~ 5 fs. As the choice of damping strength (ξ) is phenomenological, several values were tested. The results were qualitatively similar except for excess peak broadening for large values of ξ . X-ray absorption spectra with clear peaks were obtained when $\xi = 0.4 \text{ Ha}^{-1}$ for α -quartz, as this was strong enough to remove nonphysical features yet did not overbroaden peaks.

2.4. Absorption Spectra of α -Quartz. Finally, real-time TDDFT simulations were used with this finite cluster, tuned functional, and absorbing potential. Here, three weak δ -function electric field simulations were performed (x , y , z polarizations) to yield the absorption spectrum spanning valence to X-ray. The computations were performed utilizing the NWChem⁹² real-time TDDFT module,⁹³ and basis sets were selected from EMSL Basis Set Exchange.⁹⁴ All real-time simulations used a time step of $\Delta t = 0.05 \text{ au} = 0.0012 \text{ fs}$ and were run for a total of $500 \text{ au} = 12 \text{ fs}$. This step is small enough to resolve core-level oscillations around $\sim 100 \text{ eV}$. As core excitations occur at higher frequencies than the valence excitations, a smaller time step was used to obtain both valence and core oscillations in the spectrum. Convergence with Δt was checked. Each simulation used 256 2.6 GHz Xeon processors for 48 h at Louisiana State University’s HPC Facility. The computed time-dependent dipole moments are shown in Figure 5, which clearly shows the damping effect of the $i\mathbf{\Gamma}'$ potential. The resulting absorption spectra were computed from the Fourier Transforms of the time-dependent dipole moments $\mu(t)$:

$$\sigma(\omega) = \frac{4\pi\omega}{3c} \text{Im}[f_x(\omega) + f_y(\omega) + f_z(\omega)] \quad (14)$$

The time-dependent dipole moments were exponentially damped to accelerate the Fourier transform, $e^{(-t/\tau)}$, ($\tau = 75 \text{ au} = 1.8 \text{ fs}$) and padded with 10^5 zeros prior to Fourier transform.

The computed valence absorption spectra of α -quartz with and without the imaginary potential ($i\mathbf{\Gamma}'$) are shown in Figure 6. The experimental UV absorption spectrum was digitized from the work done by Chang et al.⁹⁵ The computed valence absorption spectrum qualitatively agrees with the experimental

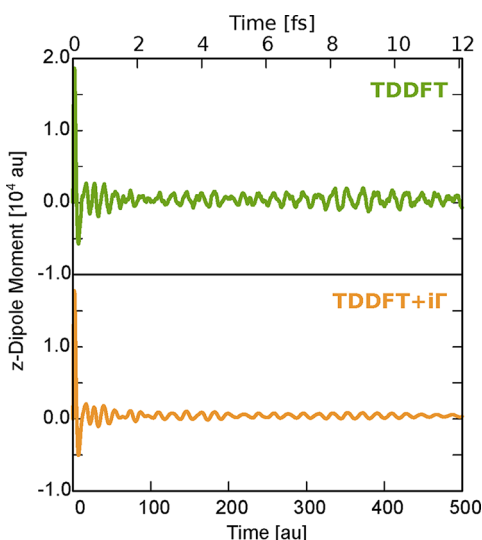


Figure 5. Time-dependent z -dipole moment with (orange) and without (green) absorbing potential.

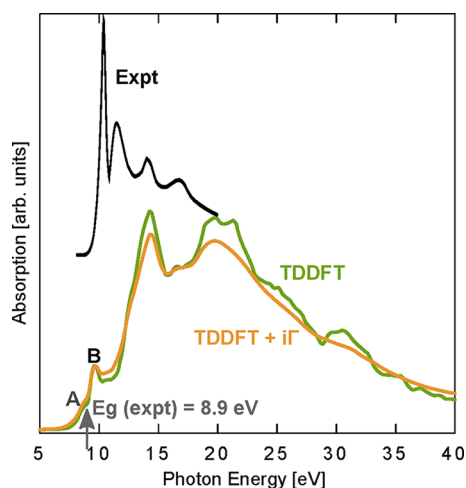


Figure 6. Computed UV absorption spectrum of α -quartz with (orange) and without (green) absorbing potential. The experimental spectrum (black) was digitized from the work done by Chang et al.⁹⁵ The experimental band gap is from the work done by Binggeli et al.⁷⁴ (digitized with permission from the American Physical Society).

spectrum⁹⁵ as well as with the density of states (DOS) of α -quartz calculated by Calabrese et al. and Binggeli et al.^{74,96} Peak A at the onset (8.4 eV) of the computed spectra is the optical gap and corresponds to the transition from O 2p to antibonding counterparts of O 2s, Si 3s, and 3p. This peak is absent in the experimental data due to vanishing transition dipole for the bulk. Peak B (9.7 eV) corresponds to the transitions from O 2s and 2p orbitals to the conduction band composed of antibonding O 2s and 2p orbitals and antibonding Si 3s and 3p orbitals. The remaining low-energy calculated valence excitation energies agree fairly well with the experimental spectrum, but the oscillator strengths are significantly different. This is likely a finite cluster size effect, where transitions are artificially localized in space, have greatly overestimated MO overlaps and thus artificially large oscillator strengths. This effect is far more pronounced in the valence, where both occupied and virtual states are somewhat

delocalized, and less so for the core, where the occupied state is essentially localized on one atom (Figure 7).

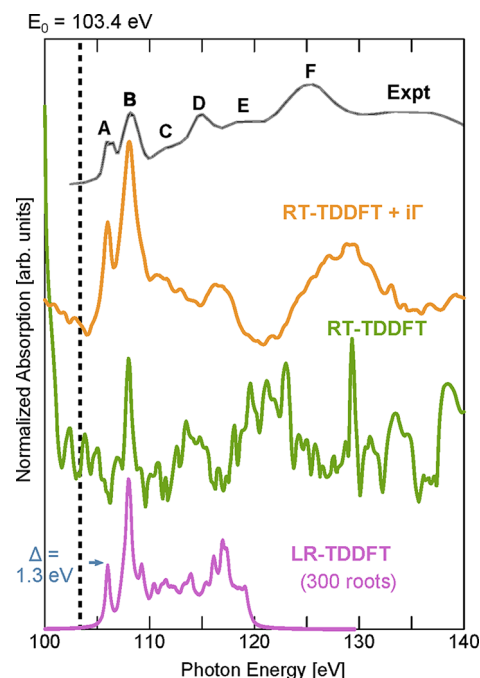


Figure 7. Computed real-time TDDFT X-ray absorption spectrum of α -quartz with (orange) and without (green) an absorbing potential, along with corresponding linear response TDDFT (purple). The three computed spectra were shifted by 1.3 eV to match with the experimental spectrum (black), which was digitized from the work done by Li et al.⁹⁷ The experimental Si 2p ionization energy (103.4 eV) is shown as a dotted line (digitized with permission from the Mineralogical Society of America).

The core absorption spectra of α -quartz obtained by RT-TDDFT computed with and without $i\Gamma$ are shown in Figure 7. Here, for clarity we subtracted the exponential continuum background from the TDDFT + $i\Gamma$ spectrum, and all TDDFT spectra were shifted by +1.3 eV to match the experiment. The parameters employed for ABC were $\epsilon_0 = 0.018$ Ha and $\xi = 0.4$ Ha⁻¹. In order to determine the corresponding transitions, LR-TDDFT was performed using the restricted excitation window approach. The LR-TDDFT spectrum obtained for 300 roots is also shown in Figure 7. These spectra are compared with the experimental Si L-edge spectrum obtained by Li et al.⁹⁷

There are clear differences in the spectra obtained from the three variants of TDDFT (LR, RT, RT+ $i\Gamma$). The RT-TDDFT without an absorbing potential is highly polluted with many nonphysical excitation, which makes interpreting this spectrum all but impossible. Adding the $i\Gamma$ results in a significantly better X-ray absorption spectrum, especially for the near-edge features, but the peaks corresponding to multiple scattering are shifted from experiment, likely due to finite basis effects or inadequacies in the absorbing potential. Also note, the low energy RT-TDDFT+ $i\Gamma$ peaks are essentially the same as the LR-TDDFT ones but differ for higher energies, mainly due to broadening from the ABC.

Finally, we discuss the origins of the various excitations. The first peak is at 105.4 eV, and as it is higher than the ionization potential of Si 2p (103.4 eV), all features in the Si L-edge up to 153.4 eV are near-edge features (XANES).⁷⁴ Peak A results from the transitions to antibonding Si 3s orbitals from Si 2p

orbitals. The spin–orbit splitting feature ($2p_{(3/2)}$, $2p_{(1/2)}$) seen in peak A in the experimental spectrum is not captured in our spectra as we do not include spin–orbit effects in our simulations. Peak B corresponds to the excitations of Si 2p electrons to antibonding 3p states. Even though $2p \rightarrow p$ transitions are atomically forbidden, this becomes dipole allowed due to the tetrahedral symmetry of α -quartz, that is, Laporte selection rule ($\Delta l = \pm 1$) is violated in this system due to its noncentrosymmetric nature. In tetrahedral symmetry, p and d orbitals transform to t_2 resulting in mixing of p and d orbitals.⁹⁸ As this will result in some d-character in p-orbitals, the $2p \rightarrow p$ transition becomes possible. Peaks C and E correspond to transitions due to multiple scattering effects where the states are not simple atomic or molecular states.⁹⁷ Peaks D and F result from the transitions to Si 3d and 3p states from Si 2p. According to the crystal field theory, in tetrahedral molecules the 3d orbitals are divided into e and t_2 states, where e states are more stable than t_2 .^{97,99} According to the experimental spectra obtained by Li et al., peak D corresponds to the transition to e states and peak F to t_2 states.⁹⁷

The A and B transitions are both very well described by TDDFT, as they are relatively localized near-edge excitations. Peaks C, D, E, and F are increasingly more difficult to capture due to both finite cluster/basis effects and limitations in the exchange-correlation function for very diffuse continuum-like virtual states.

3. CONCLUSIONS

In summary, we have computed the near- and post-edge X-ray absorption spectrum of insulators using real-time time-dependent density functional theory (RT-TDDFT). An embedded finite cluster model of α -quartz was used as an example where the spectra were computed using atom-centered basis sets and range-separated functionals. The LC-PBE0* functional was tuned to satisfy the Koopmans' ionization potential condition to find the best tuned parameters (α and γ), and the straight line behavior of the functional was also verified. The post-edge excitations were captured using real-time TDDFT with an imaginary absorbing potential. This results in a finite lifetime in low-lying unbound virtual orbitals and completely removes the nonphysical high-lying orbitals. The resulting Si L-edge spectrum was purified of spurious excitations and matches well with experimental data over the range of ~ 105 – 120 eV, i.e., approximately 15 eV above the ionization edge.

This method of computing X-ray absorption using embedded cluster models, atom-centered basis sets, tuned functionals, and absorbing boundary conditions resulted in a significantly improved spectrum over traditional TDDFT and agrees well with the experiment. Due to the difficulties in treating infinite solids with TDDFT, bulk-mimicking embedded finite cluster models are a useful tool for studying the excited-state electronic structure of materials. Embedded finite clusters with all-electron basis sets are also natural for XAS calculations and facilitate use of (tuned) hybrid DFT functionals at a more modest computational cost than planewaves or grid-based methods.

A major drawback to this approach is the choice of the molecular-orbital absorbing boundary condition, which must be picked carefully as to remove nonphysical states but not overdamp the XAS features. A more rigorous way is to use spatially dependent ABCs, but this would potentially require very large basis sets. Also, even for tuned functionals, the computed spectra are shifted from experiment by a few percent, likely due to incorrect core–hole response. Moreover, core

excitations occur at higher frequencies than valence excitations, so Δt for RT-TDDFT must be sufficiently small so that it ensures the capturing of both core and valence excitations, which requires long simulation times. Finally, even though the full absorption spectrum can be obtained in just one simulation with RT-TDDFT, the transitions corresponding to the peaks cannot be easily analyzed because extracting the orbital contributions from the time-dependent density matrix is not straightforward. Hence, LR-TDDFT is often required to assign those transitions. Despite these drawbacks, non-Hermitian real-time TDDFT offers a simple approach for near-edge XAS suitable for modeling spectroscopy and dynamics in systems ranging from organic molecules to inorganic complexes to potentially disordered solid-state materials, all without experimental parametrization.

■ ASSOCIATED CONTENT

Supporting Information

Geometry of the $\text{Si}_5\text{O}_{16}\text{H}_{12}$ cluster. This material is available free of charge via the Internet at <http://pubs.acs.org>.

■ AUTHOR INFORMATION

Corresponding Author

*E-mail: klopata@lsu.edu.

Notes

The authors declare no competing financial interest.

■ ACKNOWLEDGMENTS

This research was supported by the Louisiana Board of Regents Research Competitiveness Subprogram under contract number LEQSF(2014-17)-RD-A-03, as well as through the Louisiana State University (LSU) Office of Research and Economic Development. This material is based upon work supported by the National Science Foundation under the NSF EPSCoR Cooperative Agreement No. EPS-1003897 with additional support from the Louisiana Board of Regents. R.G.F. acknowledges support from the DOW Chemical Company and Louisiana Board of Regents. M.C.B. acknowledges support from the LSU Chancellor's Future Leaders in Research program. Portions of this research were conducted with high performance computational resources provided by Louisiana State University (<http://www.hpc.lsu.edu>). Finally, we also thank Niranjana Govind and George Stanley for helpful discussions, as well as the reviewer for useful discussions about the validity of adiabatic functionals for high-frequency fields.

■ REFERENCES

- (1) Penner-Hahn, J. E. X-ray Absorption Spectroscopy. In *Comprehensive Coordination Chemistry II*; Meyer, J. A. M. J., Ed.; Pergamon: Oxford, 2003; Chapter 2.13, pp 159–186.
- (2) Fonda, L. J. *Phys.: Condens. Matter* **1992**, *4*, 8269–8302.
- (3) Ankudinov, A.; Ravel, B.; Rehr, J.; Conradson, S. *Phys. Rev. B* **1998**, *58*, 7565–7576.
- (4) Albrecht, S.; Reining, L.; Del Sole, R.; Onida, G. *Phys. Rev. Lett.* **1998**, *80*, 4510–4513.
- (5) Shirley, E. L. *Phys. Rev. Lett.* **1998**, *80*, 794–797.
- (6) Taillefumier, M.; Cabaret, D.; Flank, A.-M.; Mauri, F. *Phys. Rev. B* **2002**, *66*, 195107–1951014.
- (7) Soininen, J.; Shirley, E. L. *Phys. Rev. B* **2001**, *64*, 165112–165116.
- (8) Gougousis, C.; Calandra, M.; Seitsonen, A. P.; Mauri, F. *Phys. Rev. B* **2009**, *80*, 075102–075109.
- (9) Besley, N. A.; Asmuruf, F. A. *Phys. Chem. Chem. Phys.* **2010**, *12*, 12024–12039.

- (10) Ankudinov, A.; Takimoto, Y.; Rehr, J. *Phys. Rev. B* **2005**, *71*, 165110–165117.
- (11) Ankudinov, A.; Nesvizhskii, A.; Rehr, J. *Phys. Rev. B* **2003**, *67*, 115120–115125.
- (12) Rehr, J. *Radiat. Phys. Chem.* **2006**, *75*, 1547–1558.
- (13) Schwitala, J.; Ebert, H. *Phys. Rev. Lett.* **1998**, *80*, 4586–4589.
- (14) Wang, Y.; Lopata, K.; Chambers, S. A.; Govind, N.; Sushko, P. *J. Phys. Chem. C* **2013**, *117*, 25504–25512.
- (15) Schultze, M.; Bothschafter, E. M.; Sommer, A.; Holzner, S.; Schweinberger, W.; Fiess, M.; Hofstetter, M.; Kienberger, R.; Apalkov, V.; Yakovlev, V. S.; Stockman, M. I.; Krausz, F. *Nature* **2013**, *493*, 75–78.
- (16) Runge, E.; Gross, E. K. U. *Phys. Rev. Lett.* **1984**, *52*, 997–1000.
- (17) Marques, M.; Gross, E. *Annu. Rev. Phys. Chem.* **2004**, *55*, 427–455.
- (18) Burke, K.; Werschnik, J.; Gross, E. *J. Chem. Phys.* **2005**, *123*, 062206–062214.
- (19) Casida, M. E. *J. Mol. Struct.: THEOCHEM* **2009**, *914*, 3–18.
- (20) Ullrich, C. A.; Yang, Z.-h. *Braz. J. Phys.* **2014**, *44*, 154–188.
- (21) Van Leeuwen, R.; Baerends, E. *Phys. Rev. A* **1994**, *49*, 2421–2431.
- (22) Tozer, D. J.; Handy, N. C. *J. Chem. Phys.* **1998**, *109*, 10180–10189.
- (23) Dreuw, A.; Weisman, J.; Head-Gordon, M. *J. Chem. Phys.* **2003**, *119*, 2943–2946.
- (24) Wasserman, A.; Maitra, N. T.; Burke, K. *Phys. Rev. Lett.* **2003**, *91*, 263001–263004.
- (25) Autschbach, J. *ChemPhysChem* **2009**, *10*, 1757–1760.
- (26) Prendergast, D.; Galli, G. *Phys. Rev. Lett.* **2006**, *96*, 215502–215505.
- (27) Uejio, J. S.; Schwartz, C. P.; Saykally, R. J.; Prendergast, D. *Chem. Phys. Lett.* **2008**, *467*, 195–199.
- (28) Yanai, T.; Tew, D. P.; Handy, N. C. *Chem. Phys. Lett.* **2004**, *393*, 51–57.
- (29) Baer, R.; Neuhauser, D. *Phys. Rev. Lett.* **2005**, *94*, 043002–043005.
- (30) Vydrov, O. A.; Scuseria, G. E. *J. Chem. Phys.* **2006**, *125*, 234109–234117.
- (31) Adamo, C.; Barone, V. *J. Chem. Phys.* **1999**, *110*, 6158–6170.
- (32) Iikura, H.; Tsuneda, T.; Yanai, T.; Hirao, K. *J. Chem. Phys.* **2001**, *115*, 3540–3544.
- (33) Tawada, Y.; Tsuneda, T.; Yanagisawa, S.; Yanai, T.; Hirao, K. *J. Chem. Phys.* **2004**, *120*, 8425–8433.
- (34) Govind, N.; Valiev, M.; Jensen, L.; Kowalski, K. *J. Phys. Chem. A* **2009**, *113*, 6041–6043.
- (35) Baer, R.; Livshits, E.; Salzner, U. *Annu. Rev. Phys. Chem.* **2010**, *61*, 85–109.
- (36) Kosloff, R.; Kosloff, D. *J. Comput. Phys.* **1986**, *63*, 363–376.
- (37) Neuhauser, D.; Baer, M. *J. Chem. Phys.* **1989**, *90*, 4351–4355.
- (38) Seideman, T.; Miller, W. H. *J. Chem. Phys.* **1992**, *96*, 4412–4422.
- (39) Jolicard, G.; Austin, E. *J. Chem. Phys. Lett.* **1985**, *121*, 106–110.
- (40) Riss, U.; Meyer, H.-D. *J. Phys. B: At. Mol. Opt. Phys.* **1993**, *26*, 4503–4536.
- (41) Sommerfeld, T.; Riss, U.; Meyer, H.-D.; Cederbaum, L. *Phys. Rev. Lett.* **1997**, *79*, 1237–1240.
- (42) Bravaya, K. B.; Zuev, D.; Epifanovsky, E.; Krylov, A. I. *J. Chem. Phys.* **2013**, *138*, 124106–124120.
- (43) Jagau, T. C.; Krylov, A. I. *J. Phys. Chem. Lett.* **2014**, *5*, 3078–3085.
- (44) Nakatsukasa, T.; Yabana, K. *J. Chem. Phys.* **2001**, *114*, 2550–2561.
- (45) Yabana, K.; Nakatsukasa, T.; Iwata, J.-I.; Bertsch, G. *Phys. Status Solidi B* **2006**, *243*, 1121–1138.
- (46) Crawford-Uranga, A.; De Giovannini, U.; Rasanen, E.; Oliveira, M.; Mowbray, D.; Nikolopoulos, G.; Karamatskos, E.; Markellos, D.; Lambropoulos, P.; Kurth, S.; Rubio, A. *Phys. Rev. A* **2014**, *90*, 033412–033419.
- (47) Zhou, Y.; Ernzerhof, M. *J. Phys. Chem. Lett.* **2012**, *3*, 1916–1920.
- (48) Reinhardt, W. P. *Annu. Rev. Phys. Chem.* **1982**, *33*, 223–255.
- (49) Moiseyev, N. *Phys. Rep.* **1998**, *302*, 212–293.
- (50) Telnov, D. A.; Sosnova, K. E.; Rozenbaum, E.; Chu, S.-I. *Phys. Rev. A* **2013**, *87*, 053406–053413.
- (51) Jensen, L.; Autschbach, J.; Schatz, G. C. *J. Chem. Phys.* **2005**, *122*, 224115–224125.
- (52) Lopata, K.; Govind, N. *J. Chem. Theory Comput.* **2013**, *9*, 4939–4946.
- (53) Yabana, K.; Bertsch, G. *Phys. Rev. B* **1996**, *54*, 4484–4487.
- (54) Yabana, K.; Bertsch, G. *Int. J. Quantum Chem.* **1999**, *75*, 55–66.
- (55) Tsolakidis, A.; Sánchez-Portal, D.; Martin, R. M. *Phys. Rev. B* **2002**, *66*, 235416–235424.
- (56) Takimoto, Y.; Vila, F.; Rehr, J. *J. Chem. Phys.* **2007**, *127*, 154114–154119.
- (57) Petersilka, M.; Gossmann, U. J.; Gross, E. K. U. *Phys. Rev. Lett.* **1996**, *76*, 1212–1215.
- (58) Casida, M. E. Time-Dependent Density Functional Response Theory for Molecules. In *Recent Advances in Density Functional Methods*; Chong, D. P., Ed.; World Scientific Publishing: Singapore, 1995; Volume 1, Chapter 5, pp 155–192.
- (59) Maitra, N. T.; Burke, K.; Woodward, C. *Phys. Rev. Lett.* **2002**, *89*, 023002–023005.
- (60) Baer, R. *J. Mol. Struct.: THEOCHEM* **2009**, *914*, 19–21.
- (61) Lopata, K.; Van Kuiken, B. E.; Khalil, M.; Govind, N. *J. Chem. Theory Comput.* **2012**, *8*, 3284–3292.
- (62) Stener, M.; Fronzoni, G.; De Simone, M. *Chem. Phys. Lett.* **2003**, *373*, 115–123.
- (63) Fronzoni, G.; Stener, M.; Reduce, A.; Decleva, P. *J. Phys. Chem. A* **2004**, *108*, 8467–8477.
- (64) Van Kuiken, B. E.; Huse, N.; Cho, H.; Strader, M. L.; Lynch, M. S.; Schoenlein, R. W.; Khalil, M. *J. Phys. Chem. Lett.* **2012**, *3*, 1695–1700.
- (65) Van Kuiken, B. E.; Valiev, M.; Daifuku, S. L.; Bannan, C.; Strader, M. L.; Cho, H.; Huse, N.; Schoenlein, R. W.; Govind, N.; Khalil, M. *J. Phys. Chem. A* **2013**, *117*, 4444–4454.
- (66) Besley, N. A.; Noble, A. *J. Phys. Chem. C* **2007**, *111*, 3333–3340.
- (67) De Francesco, R.; Stener, M.; Fronzoni, G. *J. Phys. Chem. C* **2007**, *111*, 13554–13563.
- (68) De Francesco, R.; Stener, M.; Fronzoni, G. *Phys. Chem. Chem. Phys.* **2009**, *11*, 1146–1151.
- (69) Bunău, O.; Joly, Y. *Phys. Rev. B* **2012**, *85*, 155121–155132.
- (70) Bunău, O.; Joly, Y. *J. Phys.: Condens. Matter* **2012**, *24*, 215502–215506.
- (71) Fronzoni, G.; De Francesco, R.; Stener, M. *J. Phys. Chem. B* **2005**, *109*, 10332–10340.
- (72) Fronzoni, G.; De Francesco, R.; Stener, M.; Causa, M. *J. Phys. Chem. B* **2006**, *110*, 9899–9907.
- (73) De Francesco, R.; Stener, M.; Causà, M.; Toffoli, D.; Fronzoni, G. *Phys. Chem. Chem. Phys.* **2006**, *8*, 4300–4310.
- (74) Binggeli, N.; Troullier, N.; Martins, J. L.; Chelikowsky, J. R. *Phys. Rev. B* **1991**, *44*, 4771–4777.
- (75) Yin, K.; Lin, H.; Cai, Q.; Zhao, Y.; Lee, S.-T.; Hu, F.; Shao, M. *Nanoscale* **2013**, *5*, 12330–12334.
- (76) Que, R.; Shao, M.; Wang, S.; Ma, D. D. D.; Lee, S.-T. *Nano Lett.* **2011**, *11*, 4870–4873.
- (77) Kasrai, M.; Fleet, M.; Bancroft, G.; Tan, K.; Chen, J. *Phys. Rev. B* **1991**, *43*, 1763–1772.
- (78) Will, G.; Bellotto, M.; Parrish, W.; Hart, M. *J. Appl. Crystallogr.* **1988**, *21*, 182–191.
- (79) Sauer, J. *Chem. Rev.* **1989**, *89*, 199–255.
- (80) Henkelman, G.; Arnaldsson, A.; Jónsson, H. *Comput. Mater. Sci.* **2006**, *36*, 354–360.
- (81) Sanville, E.; Kenny, S. D.; Smith, R.; Henkelman, G. *J. Comput. Chem.* **2007**, *28*, 899–908.
- (82) Tang, W.; Arnaldsson, A.; Chill, S. T.; Henkelman, G. Bader Charge Analysis. <http://theory.cm.utexas.edu/henkelman/research/bader> (accessed March 2014).
- (83) Tang, W.; Sanville, E.; Henkelman, G. *J. Phys.: Condens. Matter* **2009**, *21*, 084204–084210.

- (84) Wiberg, K. B.; Rablen, P. R. *J. Comput. Chem.* **1993**, *14*, 1504–1518.
- (85) Casida, M. E.; Salahub, D. R. *J. Chem. Phys.* **2000**, *113*, 8918–8935.
- (86) Hirata, S.; Zhan, C.-G.; Aprà, E.; Windus, T. L.; Dixon, D. A. *J. Phys. Chem. A* **2003**, *107*, 10154–10158.
- (87) Srebro, M.; Autschbach, J. *J. Chem. Theory Comput.* **2011**, *8*, 245–256.
- (88) Perdew, J. P.; Parr, R. G.; Levy, M.; Balduz, J. L., Jr. *Phys. Rev. Lett.* **1982**, *49*, 1691–1694.
- (89) Cohen, A. J.; Mori-Sánchez, P.; Yang, W. *Science* **2008**, *321*, 792–794.
- (90) Mori-Sánchez, P.; Cohen, A. J.; Yang, W. *Phys. Rev. Lett.* **2008**, *100*, 146401–146404.
- (91) Ruso, J. M.; Gravina, A. N.; D'Elia, N. L.; Messina, P. V. *Dalton Trans.* **2013**, *42*, 7991–8000.
- (92) Valiev, M.; Bylaska, E. J.; Govind, N.; Kowalski, K.; Straatsma, T. P.; Van Dam, H. J.; Wang, D.; Nieplocha, J.; Apra, E.; Windus, T. L. *Comput. Phys. Commun.* **2010**, *181*, 1477–1489.
- (93) Lopata, K.; Govind, N. *J. Chem. Theory Comput.* **2011**, *7*, 1344–1355.
- (94) Schuchardt, K. L.; Didier, B. T.; Elsethagen, T.; Sun, L.; Gurumoorhi, V.; Chase, J.; Li, J.; Windus, T. L. *J. Chem. Inf. Model.* **2007**, *47*, 1045–1052.
- (95) Chang, E. K.; Rohlfing, M.; Louie, S. G. *Phys. Rev. Lett.* **2000**, *85*, 2613–2616.
- (96) Calabrese, E.; Fowler, W. B. *Phys. Rev. B* **1978**, *18*, 2888–2896.
- (97) Li, D.; Bancroft, G.; Kasrai, M.; Fleet, M.; Secco, R.; Feng, X.; Tan, K.; Yang, B. *Am. Mineral.* **1994**, *79*, 622–632.
- (98) Hansen, P. L.; Brydson, R.; McComb, D. W. *Microsc. Microanal. Microstruct.* **1992**, *3*, 213–219.
- (99) Liu, Z.; Cutler, J.; Bancroft, G.; Tan, K.; Cavell, R.; Tse, J. *Chem. Phys.* **1992**, *168*, 133–144.